Morphological and crystallographic anisotropy of severely deformed commercially pure aluminium by three-dimensional electron backscatter diffraction

Naghdy, Soroosh; Pirgazi, Hadi; Verleysen, Patricia; Petrov, Roumen; Kestens, Leo

Morphological and crystallographic anisotropy of severely deformed commercially pure aluminium by three-dimensional electron backscatter diffraction

Soroosh Naghdy,[a]* Hadi Pirgazi,[a] Patricia Verleysen,[a] Roumen Petrov[a,b] and Leo Kestens[a,b]

[a]EEMMeCS Department, Research Group Materials Science and Technology, Ghent University, Belgium, and [b]Department of Materials Science and Engineering, Delft University of Technology, The Netherlands. *Correspondence e-mail: soroosh.naghdy@ugent.be

The aim of this paper is to examine the morphological and crystallographic anisotropy that develops during high-pressure torsion (HPT) processing. Commercially pure aluminium was subjected to monotonic HPT deformation at room temperature. The microstructure and texture were studied by large-area electron backscatter diffraction (EBSD) scans. Three-dimensional EBSD scans served to scrutinize the morphological anisotropy and local texture. It was observed that two distinct stages of grain fragmentation and saturation occur during processing. Grains exhibited an ellipsoidal shape rather than an equiaxed one. The major axes of the ellipsoids showed a favorable orientation at the steady-state stage: an almost 20° inclination towards the shear direction. The global texture was characterized by typical shear components of face-centered cubic metals at both stages. However, the local texture revealed a preferential fragmentation pattern in the first stage: orientations in the vicinity of ideal fibers became less heavily fragmented while non-ideal orientations broke up more severely. This phenomenon was linked with the lattice rotation required to bring an initial orientation close to a stable one. Although the texture weakened considerably in the fragmentation stage, the texture index did not further decrease in the saturation stage. Saturation of texture, grain refinement and formation of microstructure are discussed in the light of different microstructural coarsening mechanisms.

1. Introduction

It has been proven that both the strength and the toughness of polycrystalline metals can be improved by grain refinement. Bulk nano-structured and ultrafine-grained (UFG) metallic materials can be efficiently manufactured by severe plastic deformation (SPD) (Valiev *et al.*, 2000; Zhu *et al.*, 2012). Amongst various available SPD techniques, equal-channel angular pressing (ECAP) and high-pressure torsion (HPT) are the most investigated processes on bars and disc-shaped samples, respectively (Zhilyaev & Langdon, 2008). In both cases, the application of an extensive hydrostatic pressure allows deformation of a sample without any concomitant change of its cross section. The main advantage of HPT processing is that a practically unlimited magnitude of strain can be imposed in one single operation. Furthermore, it has been used successfully for deformation of relatively brittle materials at low temperatures (Langdon, 2013).

In the HPT process two distinct stages of microstructural evolution can be distinguished, with a transition phase in between: the grain fragmentation stage (at equivalent strains between 1 and 10), followed by the saturation stage (Pippan *et*

15 um   15 um
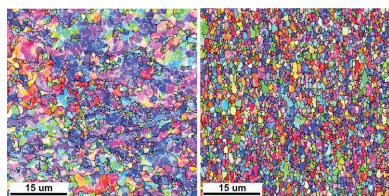
al., 2010). Interaction of grains with neighboring ones must allow the continuity of the structure during deformation. As a consequence, the stress distribution inside a grain follows a heterogeneous pattern, leading to the activation of different sets of slip systems and the development of specific crystallographic rotations in different regions of the initially homogenous crystallite volume. As the deformation proceeds, the misorientation between adjacent volume units increases, until they can be distinguished as different grains. At very large strains (between 10 and 30), a dynamic balance between generation and annihilation of defects is observed, which gives rise to the so-called saturation regime (Setman *et al.*, 2008; Van Swygenhoven *et al.*, 2002; Zhilyaev *et al.*, 2001). Observations of the saturated microstructure reveal that after ECAP – route A experiments a deviation from equi-axed grains might exist in different directions (Pippan *et al.*, 2010). Also, monotonically processed HPT samples of Al–3%Mg alloy show an elongated microstructure at 77 and 473 K (Bachmaier *et al.*, 2010). Furthermore, during HPT processing at different temperatures, the grains' long axes might show a favorable inclination towards the shear direction. This deviation has not been quantified yet and its origin is not very well understood, since a coincidence between the shear direction and the long axes of grains is expected after very severe strain magnitudes.

The occurrence of the steady-state stage is often linked with special mechanisms, which result in motion of grain boundaries (GBs), and coalescence or growth of grains. This GB migration plays an important role during dynamic recrystallization (DRX) (Pippan *et al.*, 2010). Two types of DRX are well documented in aluminium: discontinuous DRX (DDRX) and continuous DRX (CDRX). DDRX is the classical recrystallization mechanism in which nucleation is followed by growth, while CDRX operates by progressive accumulation of dislocations in subgrain boundaries, associated with a gradual increase of misorientation and formation of new grain boundaries (Chovet *et al.*, 2000; Gourdet & Montheillet, 2002). The difference in free energy on either side of a GB provides the driving force for migration of atoms. Purity has been reported to play an important role with regard to the DRX behavior of aluminium (Gourdet & Montheillet, 2003; Montheillet & Le Coze, 2002). Hot compression experiments were carried out on aluminium single crystals and it was shown that, in aluminium of 99.99% purity, the unstable $\langle 111 \rangle$ orientations fragment. These orientations, however, underwent DDRX with an increase of purity to 99.999%. During simple shear deformation, it is possible for orientations close to stable positions to rotate away from the stable orientation. Barnett & Montheillet (2002) used the asymmetric convergent/divergent nature of the rotation field to simulate generation of new high-angle grain boundaries in commercially pure aluminium during hot torsion. This phenomenon was reported to have the potential to transform randomly generated low-angle grain boundaries (LAGBs) into high-angle boundaries (HAGBs) and result in grain fragmentation.

However, the occurrence of DRX in aluminium during cold deformation is more controversial (Kaibyshev *et al.*, 2006; Sakai *et al.*, 2009). There have been sufficient experimental reports of DDRX in aluminium of very high purity (Kassner & Evangelista, 1995; Skrotzki Scheerbaum, Oertel, Brokmeier *et al.*, 2007). Calorimetric investigations during torsion deformation under liquid nitrogen show two distinguished peaks: the first one due to recovery of point defects and the second one due to recrystallization (Haessner & Schmidt, 1993). As a consequence of the occurrence of DDRX a change in mechanical properties should be observed. It is reported that the hardness of high-purity aluminium sharply drops during SPD processing, while only a plateau is recognized in low-purity aluminium (Kawasaki, 2014). It is now the general consensus that the presence of impurities restricts DDRX in low-purity aluminium, and if recrystallization occurs, grain refinement might be dominated by CDRX (Hallberg *et al.*, 2010).

Other microstructural coarsening mechanisms have been reported as well. Numerous experimental studies report stress-induced boundary migration, which is basically the motion of GBs as a response to an external mechanical stress field (Gianola *et al.*, 2006; Haslam *et al.*, 2003). This phenomenon is also termed as shear migration coupling (Gianola *et al.*, 2006; Haslam *et al.*, 2003; Molodov *et al.*, 2007; Pippan *et al.*, 2010; Winning, 2007). Stress-dependent grain growth has been observed in bicrystals of Zn (Sheikh-Ali & Szpunar, 1998), Al (Fukutomi *et al.*, 1991) and Au (Babcock & Balluffi, 1989). Atomistic modelling for 25 columnar grains with an average grain size of about 15 nm also predicts stress-enhanced grain growth (Haslam *et al.*, 2003). Recent experiments on nanocrystalline 99.999% purity aluminium thin films emphasize the importance of stress-assisted grain growth at room temperature (Legros *et al.*, 2008). Cahn & Taylor (2004) performed molecular dynamics simulations and published a theoretical formulation (Cahn *et al.*, 2006) describing that normal and parallel motion of GBs is almost compelled to be coupled. Micrometre-grain-sized aluminium with 99.5% purity has shown shear migration coupling and grain growth during an *in situ* transmission electron microscopy (TEM) straining experiment at a temperature of 623 K (Caillard *et al.*, 2009; Mompiou *et al.*, 2009). It is observed that with the application of stress GBs start to move. When the stress is kept constant, the movement stops, and, as soon as a new increment of stress is applied, GB movement starts again. Tensile experiments were performed on 99.98% purity Al bicrystals at a temperature of 593 K, and it was shown that in $\langle 100 \rangle$ tilt GBs the shear-stress-induced migration and the lateral translation of grains are perfectly coupled (Molodov *et al.*, 2007). As opposed to DRX, which is a diffusional mechanism, shear-coupled grain growth might take place by athermal shear, and it has been shown that diffusion and coupled GB motion do not exclude each other (Cahn *et al.*, 2006).

Coalescence and growth of grains might also occur as a result of grain boundary sliding (GBS) (Van Swygenhoven *et al.*, 2002). GBS, reported in a study on ECAP-processed aluminium, is proposed as the deformation mechanism accounting for superplasticity (Chinh *et al.*, 2006). It was observed that, in nanocrystalline nickel, GBS and grain rotation lead to growth of grains (Shan *et al.*, 2004). The existence

of non-equilibrium boundaries with a high dislocation density in their vicinity favors GBS. A change from pure dislocation glide to GBS is also observed for pure copper (Kozlov *et al.*, 2004), aluminium and its alloys (Huang & Langdon, 2003; Xu *et al.*, 2003), and iron (Valiev *et al.*, 1996) at the sub-micrometre scale. Furthermore, GBS is predicted by molecular dynamics simulations at low temperatures and high strain rates for nano-structured materials with an average grain size of 10 nm (Van Swygenhoven *et al.*, 1999).

The effect of severe plastic deformation on the texture evolution of HPT-processed metals is of great interest. Although the material flow in HPT is more complex than in a classical torsion test, most often a simple shear deformation mode is assumed (Orlov *et al.*, 2009). Experimental results for face-centered cubic (f.c.c.) metals, processed by simple shear, suggest the appearance of a relatively weak texture. It is observed that the fraction of grains exhibiting a particular orientation is prone to change, as new grains enter a given texture component and other grains leave it dynamically (Naghdy, Kesten *et al.*, 2016; Tóth *et al.*, 1989). An interactive effect of texture change and fragmentation is expected in the fragmentation stage. In the steady-state stage, however, the evolution of texture is no longer affected by fragmentation effects but might be influenced by characteristics of the saturation regime. An orientation-dependent shear-coupled grain growth during cold rolling of a nanocrystalline Ni–Fe alloy was reported by Li *et al.* (2016). An attempt was made to include the effect of grain growth in a Taylor-type relaxed-constraints viscoplastic polycrystal model, in such a way that it accounts for cigar-shaped grains. It was shown that the shape of grains plays an important role in the texture evolution (Li *et al.*, 2016). A correlation between the evolution of texture in the fragmentation and saturation regimes and the mechanisms that control the severity of grain refinement has not yet been reported.

In the present work, SPD by HPT is applied to a bulk commercially pure aluminium alloy with the aim of studying the morphological and crystallographic anisotropy with increasing shear strain. The deformed samples, up to an equivalent strain of 50, were characterized by conventional and three-dimensional (3D) electron backscatter diffraction (EBSD). EBSD scans were performed in different zones of the HPT material discs. In order to investigate the texture formation, zones of equal equivalent strain were merged together to produce a statistically reliable area. 3D-EBSD scans were performed during the fragmentation, saturation and transitional stages. Subsequently, an orientation-selective fragmentation mechanism of grains together with their morphological anisotropy was studied, whereby the formation of microstructure and texture in the two deformation regimes are discussed in detail.

2. Material and experimental procedure

2.1. Material and sample processing

A commercially pure aluminium alloy with the composition Al–0.28% Fe–0.05% Si–0.05% Cu (wt%) was used for this study. The cast material with 25 mm thickness was initially cold rolled to 1.2 mm thickness and then annealed at 773 K (500°C) for 30 s, resulting in a fully recrystallized structure with mean grain size of 85 μm. Discs with 15 mm diameter were cut out of the sheet and deformed by HPT processing under so-called semi-constrained conditions (Hohenwarter *et al.*, 2009) at room temperature. The applied force was maintained at a constant value of 450 kN, corresponding to a nominal pressure of 2.5 GPa, and the rotational speed of the tool was maintained at 1 r min^{-1}.

In order to define the sample geometry, a cylindrical reference system is adopted with r, Θ and Z representing the radial (RD), circumferential and thickness directions, respectively (*cf.* Fig. 1). The Θ and Z directions correspond to the shear direction (SD) and shear plane normal (SPN), respectively (Valiev *et al.*, 2000).

The equivalent strain under HPT processing was estimated by the simplified von Mises strain equation:

$$\varepsilon_{\mathrm{eq}} = \frac{\gamma}{3^{1/2}} = \frac{1}{3^{1/2}}\frac{r}{h}\Phi \qquad (1)$$

with γ the engineering shear strain, r the radius, h the initial thickness of the specimen and Φ the angle of rotation in radians (Jonas & Aranas, 2014). Revolutions of 1/2, 1 and 5, corresponding to equivalent strains of up to 50, were imposed on the discs. To preserve the strain-induced structure, prior to microstructural examination the deformed samples were stored in a freezer at 253 K.

2.2. Microstructure and texture characterization

Prior to the EBSD measurements, the discs were first finely polished using 3 and 1 μm alumina solutions and then electropolished by A2 Struers electrolyte, under a voltage of 48 V for 20 s at 295 K. An EDAX-TSL EBSD system attached to an FEI environmental scanning electron microscope (QUANTA 450 with a field emission gun), operated at an accelerating voltage of 15 kV, a working distance of 16 mm and a tilt angle of 70°, was used for the measurements. Microstructural and textural studies were carried out with step sizes of 0.1 and 1 μm, respectively. EBSD scans were performed on both r–Θ and Θ–Z planes (*cf.* Fig. 1). The location of observation is in the middle region of the disc height, at a constant radius of 3 mm for all three samples, which corresponds to equivalent strains of 5, 10 and 50. The *OIM* software (EDAX;
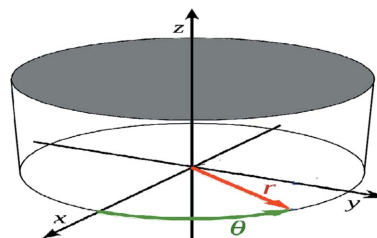
Figure 1
Representation of cylindrical coordinate system: r, Θ and Z correspond to the radial direction, shear direction and shear plane normal direction, respectively. r–Θ and Θ–Z planes are distinguished by their normal directions: Z and r.

Table 1
Dimension and resolution of the captured three-dimensional volumes.

Sample	In-plane step size (nm)	Out of plane step size (nm)	Number of parallel sections	Total volume (μm^3)	Number of grains
1: $\varepsilon_{eq} = 5$	100	100	100	1000	250
2: $\varepsilon_{eq} = 10$	50	100	50	125	1270
3: $\varepsilon_{eq} = 50$	50	100	50	125	2090

http://www.edax.com) was used to determine the mean grain size, whereby cut-off angles of 1.0 and 15.0° were considered for the minimum boundary misorientation and high-angle grain boundaries, respectively.

For the representation of orientation distribution functions (ODFs), the *MTEX* software (http://mtex-toolbox.github.io/) was used, in combination with *MTM-FHM* (Van Houtte, 2004) for calculation of the texture index. The reference system employed here for ODF calculation is axis 1 ∥ the shear direction; axis 2 ∥ the shear plane normal and axis 3 ∥ the radial axis of the disc. To obtain representative data for texture study at each given strain, an area of 1 mm² was scanned. This area is built by merging eight measurements conducted on zones with equal distance from the center of the disc along the horizontal, vertical and diagonal lines intersecting the disc center.

In order to study the morphological anisotropy of the grain structure and the fragmentation during the HPT processing, the 3D-EBSD technique was employed to obtain three-dimensional orientation maps of the microstructures. An FEI Nova 600 Nanolab Dual-Beam microscope, which combines a field emission gun scanning electron microscope (equipped with an Oxford HKL fast acquisition EBSD system) with a focused ion beam (FIB) system, was used to perform 3D-EBSD measurements by FIB serial sectioning. This is a technique based on serial sectioning, which involves the successive removal of parallel layers of the sample, followed by subsequent EBSD mapping. With this approach, a series of closely spaced parallel two-dimensional sections reveal the third dimension of the microstructure.

Prior to the 3D-EBSD measurement, two adjacent faces of the samples were mechanically polished to create an orthogonal angle with a sharp edge. The volume of interest was located on the edge between these two polished surfaces. The 3D-EBSD started with a rough cut (using 30 kV, 3 nA FIB) on this edge to form a more precise orthogonal angle. In order to obtain high-quality EBSD patterns, a low ion beam current of 0.5 nA at 30 kV was employed to remove and polish each individual section. The sections on which the EBSD was measured were parallel to the Θ–Z plane of the sample. The total captured volume and more details of these measurements are presented in Table 1.

The entire 3D-EBSD measurement workflow was fully automated and controlled using the Oxford HKL fast acquisition software. The collected three-dimensional stacks were post-processed by employing the Oxford HKL 3D viewer software. The post-processing procedure includes alignment of the parallel sections, cleanup of the raw data, and employment of cut-off angles of 1 and 15.0° for the minimum boundary misorientation and high-angle grain boundaries, respectively. Subsequently, grain aspect ratios were calculated.

3. Experimental results

3.1. Microstructure and texture before HPT processing

Fig. 2 shows the inverse pole figure (IPF) map and the ODF sections of the initial microstructure obtained from the EBSD
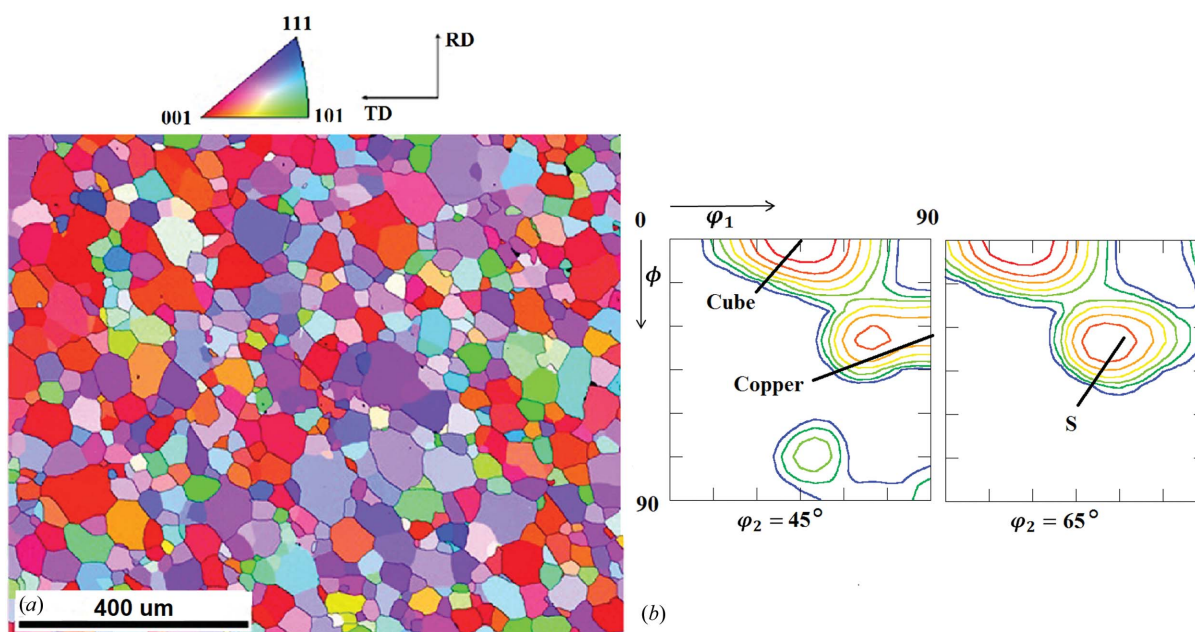
Figure 2
Microstructure (*a*) and texture (*b*) of the initial material before HPT processing. (*a*) Normal direction IPF map representing the microstructure and grain orientations. (*b*) ODF in sections at $\varphi_2 = 45$ and 65°; contours are 0.6, 1, 1.6, 2.4, 3.8, 5.9, 9.2 and 14.3 times random distribution.

measurement. Equi-axed grains with a mean grain size of ∼85 µm are observed, while high-angle grain boundaries occupy about 80% of the entire GB length. The ODF sections show a typical aluminium recrystallization texture, which is dominated by the cube texture component {100}⟨001⟩, added with retained rolling components in the vicinity of Cu {112}⟨111⟩ and S {231}⟨346⟩ (Samajdar et al., 1999).

3.2. Microstructure and morphology after HPT processing

EBSD maps illustrating the microstructural evolution from top surface observation (r–Θ plane) are shown in Fig. 3. A cleanup procedure of eliminating pixels with confidence index less than 0.1, followed by a grain dilation correction consisting of a grain tolerance angle of 5° and a minimum grain size of 2 pixels, was employed in data processing. The individual grains are defined as regions exhibiting a misorientation of 15° and containing a minimum of 5 pixels. Grains are designated according to their crystallographic directions relative to the SPN, and LAGBs (1 < LAGBs < 15°) and HAGBs (15 ≤ HAGBs) are highlighted with solid white and black lines, respectively. At an accumulated strain of 5, a significant grain refinement is visible in the microstructure (Fig. 3a) as the
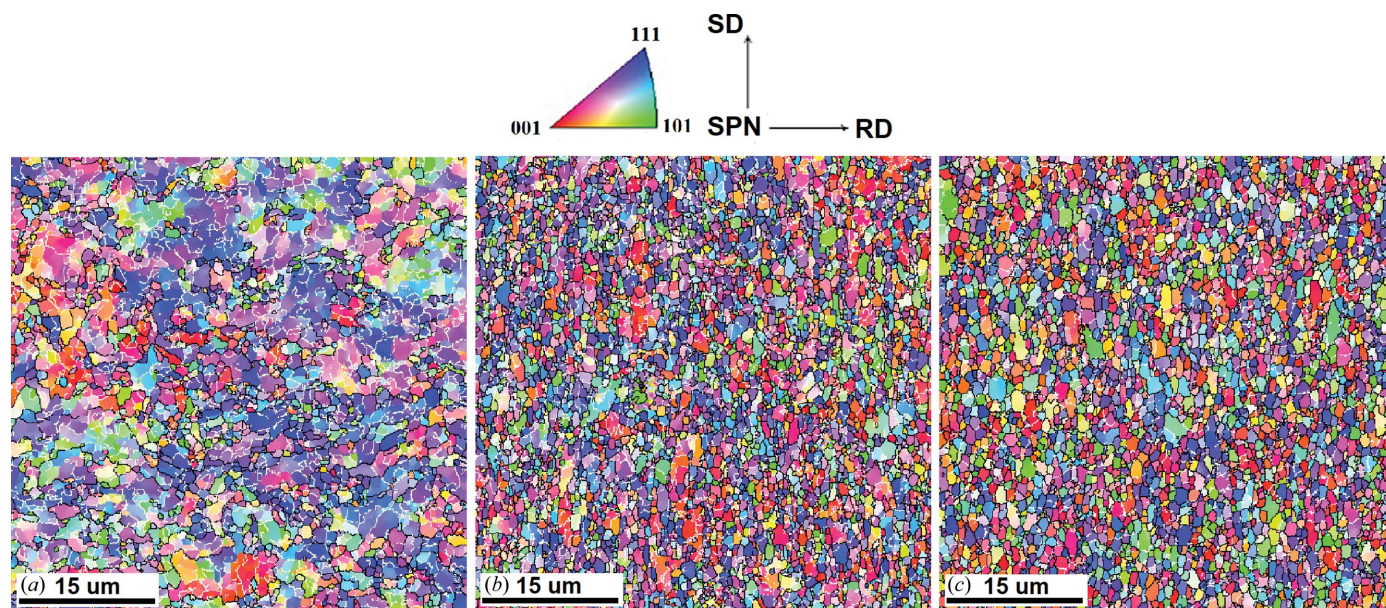
Figure 3
IPF maps measured on the r–Θ plane, depicting the grain structures at equivalent strains of (a) 5, (b) 10 and (c) 50. Individual grains are colored according to crystal direction coinciding with the SPN direction, cf. attached color key.
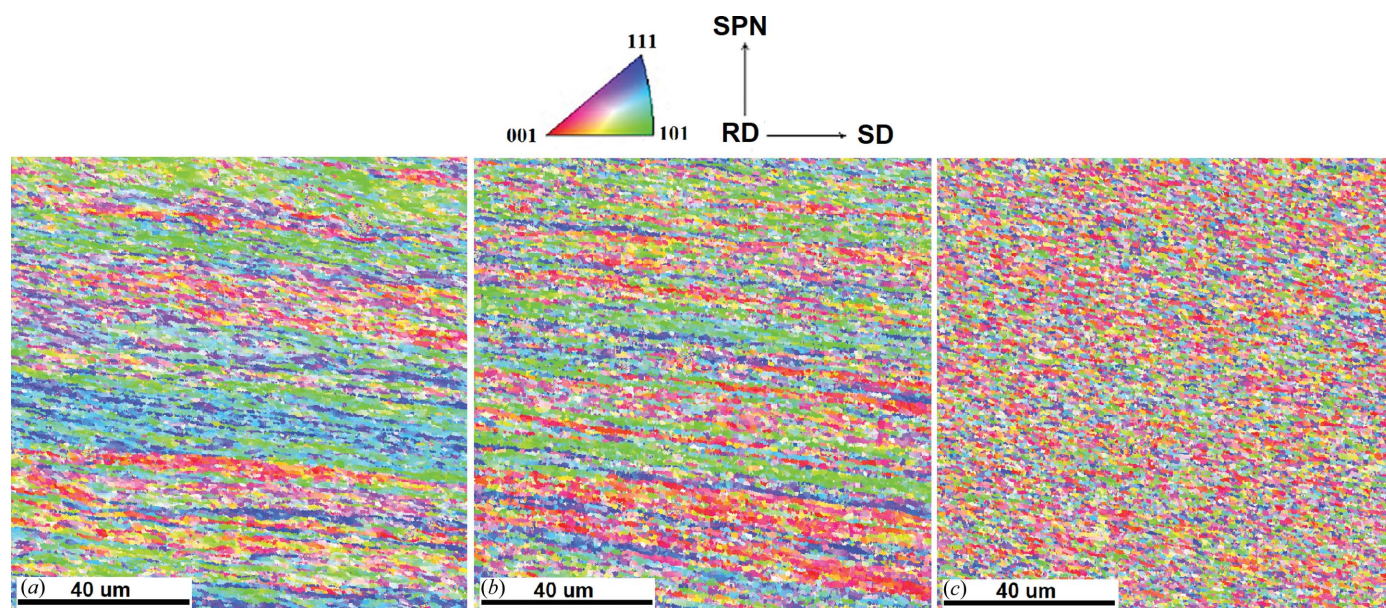
Figure 4
IPF maps measured on the Θ–Z plane, depicting the grain structures at equivalent strains of (a) 5, (b) 10 and (c) 50. Individual grains are colored according to crystal direction coinciding with the RD direction, cf. attached color key.

Table 2
Statistical analysis of grain shapes at equivalent strains of 5, 10 and 50 ($a > b > c$).

		Experiment			Theory
Equivalent strain	a (µm)	a/b	b/c	a/c	a/c
5	4.07 ± 1.08	1.88 ± 0.63	3.36 ± 2.36	6.22 ± 4.90	77
10	1.29 ± 0.42	1.84 ± 0.67	2.74 ± 1.05	4.94 ± 2.46	300
50	1.22 ± 0.38	1.82 ± 0.68	2.42 ± 0.94	4.32 ± 2.24	7500

average grain size has decreased from ∼85 to ∼7 µm. The microstructure consists of coarser and smaller grains, the smaller grains appearing mostly in the vicinity of existing HAGBs. At an accumulated strain of 10, the initial grains have completely vanished and the microstructure becomes finer with an average grain size of ∼1.5 µm. This strain might be considered as a transition from fragmentation to saturation because further significant grain refinement is not observed at higher strains. Finally at a strain of 50, well in the saturation zone, a very fine microstructure with an average size of ∼1 µm and a uniform distribution is observed.
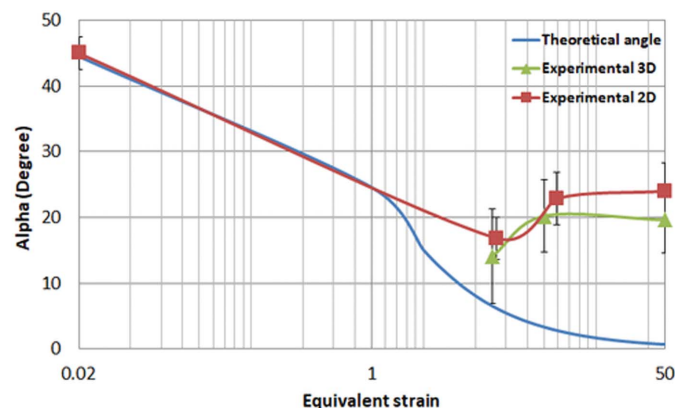

Figure 5
Theoretical and experimental directionality of grains towards the shear direction as a function of imposed equivalent strain.

EBSD measurements on the Θ–Z planes are illustrated in Fig. 4. The directionality of the grains is clearly depicted by IPF maps at different deformation levels. The Θ–Z plane's EBSD measurements and 3D-EBSD scans were analyzed to estimate the directionality of the grain structure. The angle α between the major axis of an average fitted ellipsis/ellipsoid and the shear direction was calculated at strain levels of 5, 10 and 50 (cf. Fig. 5). A theoretical angle is displayed in Fig. 5 as well; details of this calculation are discussed in §4.1.

Ellipsoids were statistically analyzed in order to calculate the morphological anisotropy of the grain shape at different strain amplitudes. Results of this analysis are represented in Table 2, with a, b and c representing the major, middle and minor lengths of an average fitted ellipsoid, respectively. The theoretical ratio between major and minor axes of an ellipsoid is shown as well; details of this calculation are discussed in §4.1.

3.3. Texture after HPT processing

The development of the torsion texture can be conveniently described in terms of the $\{hkl\}\langle uvw \rangle$ notation in such a way that $\{hkl\}$ is parallel to the shear plane r–Θ and $\langle uvw \rangle$ is the crystal direction that is parallel to the shear direction Θ. Ideal shear texture components of f.c.c. metals together with their corresponding Taylor factors are listed in Table 3 (Tóth *et al.*, 1989, 1992).

Fig. 6 depicts the results of large-area EBSD scans. Shear textures are illustrated in the form of ODFs, since the overlap between the ideal components in the pole figures disturbs the estimation of individual intensities. Using the ODF key, it can be concluded that all ideal components of shear deformation are present at a strain of 5, and the initial recrystallization texture (Fig. 2b) has been replaced by a newly developed deformation texture. The ODF maximum decreases by a factor of two when deformation is further increased to a strain of 10. At a strain level of 50, a similar texture to that of a strain of 10 is observed. The texture index (TI) is calculated to quantify the strength of evolved textures (cf. Table 4). This
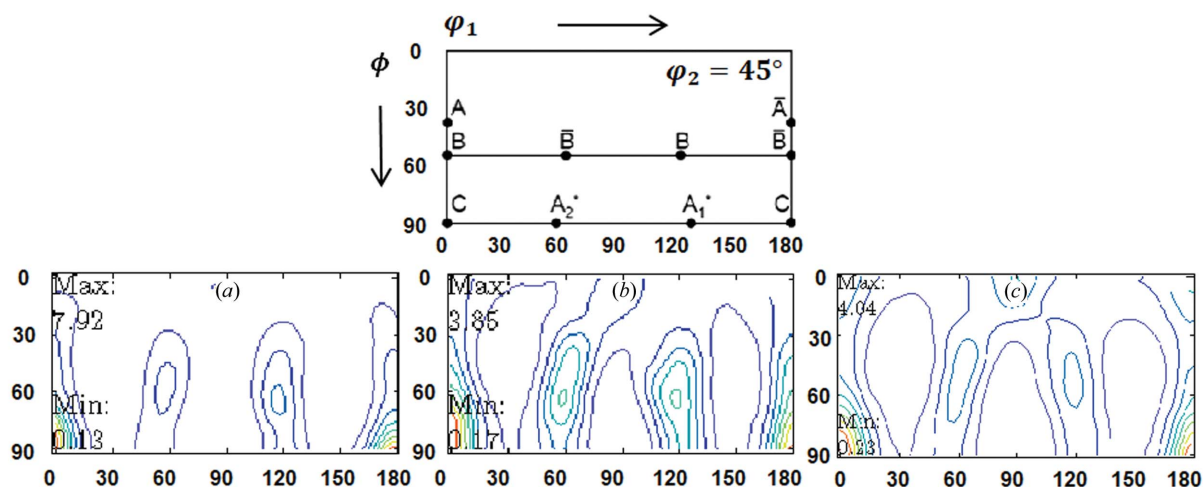

Figure 6
Experimental shear textures at equivalent strains of (a) 5, (b) 10 and (c) 50 ($\varphi_2 = 45°$ sections of the ODF) obtained by large-area EBSD scans.

Table 3
Ideal texture components observed in f.c.c. materials after simple shear deformation (Tóth *et al.*, 1989, 1992).

| Component	$\{hkl\}\langle uvw\rangle$	Euler angles (°)	Taylor factor
A	$(1\bar{1}\bar{1})[110]$	0–35.26–45	1
$\bar{A}$	$(\bar{1}11)[\bar{1}\bar{1}0]$	180–35.26–45	1
A_1^*	$(\bar{1}\bar{1}1)[112]$	35.37–45–0	1.15
		125.37–90–45	
A_2^*	$(11\bar{1})[112]$	144.74–45–0	1.15
		54.74–90–45	
B	$(\bar{1}12)[110]$	0–54.74–45	1.41
		120–54.74–45	
$\bar{B}$	$(1\bar{1}\bar{2})[\bar{1}\bar{1}0]$	60–54.74–45	1.41
		180–54.74–45	
C	$(100)[110]$	90–45–0	1.73
		0–90–45	

$\langle 111 \rangle$ or A fiber $\{111\}\langle uvw \rangle$
$\langle 110 \rangle$ or B fiber $\{hkl\}\langle 110 \rangle$

Table 4
Calculated texture index at different strain levels.

	Annealed	$\varepsilon_{eq} = 5$	$\varepsilon_{eq} = 10$	$\varepsilon_{eq} = 50$
Texture index	4.91	1.69	1.38	1.30
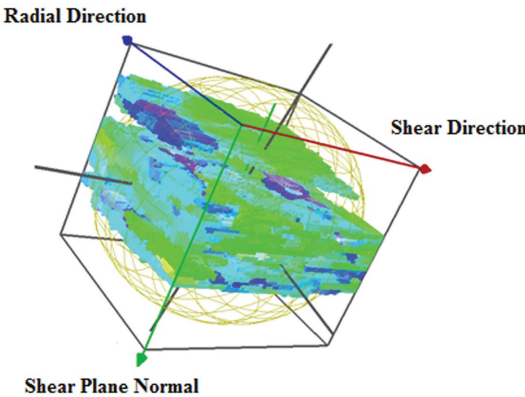
Figure 7
3D-EBSD grain map representation of intertwined grains No. 1 and No. 2, designated, respectively, by colors blue and green, occupying 38% of the scanned volume.
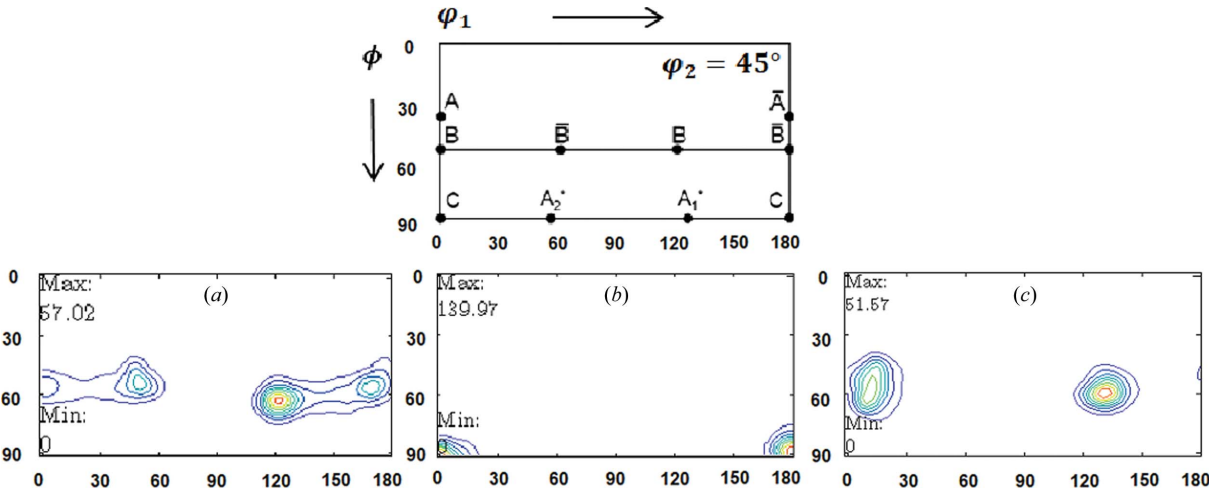
parameter is defined as the integral of the square of the orientation distribution function over the entire orientation space, and it has a value close to unity or infinity for a random texture or a single component, respectively (Kocks *et al.*, 2000).

3D-EBSD results at a strain level of 5 were used to study the local texture evolution in the fragmentation stage. A total volume of 1000 μm³ was scanned, which contains about 250 grains. The individual grains are defined as regions having a misorientation of 15° and containing a minimum of 27 voxels. A discrepancy was observed between grain sizes as about 46% of the volume is occupied by three large grains. Grains No. 1 and No. 2 (Fig. 7) and No. 3 occupy 380 and 80 μm³ of space, respectively, while the rest of the volume is occupied by 247 grains. ODF sections of $\varphi_2 = 45$ deg are shown in Fig. 8. Grains No. 1 and No. 2 are precisely centered on fiber B, while grain No. 3 is perfectly positioned at orientation C, and the remaining volume is scattered around the B component.

4. Discussion

4.1. Microstructure formation and evolution of morphological anisotropy

At a strain of 5, a mixture of LAGBs and emerging HAGBs is observed. The grain size has diminished by one order of magnitude, and HAGBs appear as an extension of LAGBs. This is an indication of grain fragmentation, occurring because of a discrepancy in lattice rotations between neighboring elements within a grain. Observation of the microstructure from the top surface suggests that grains are fairly equi-axed at strain levels of 10 and 50. However, 3D-EBSD measurements reveal that they have an ellipsoidal shape. The rotation of a volume element, and evolution of its shape in simple shear deformation, could be estimated theoretically (Canova *et al.*, 1982).

As a consequence of shearing (Fig. 9), an inscribed circle within an elemental square transforms into an ellipse within a
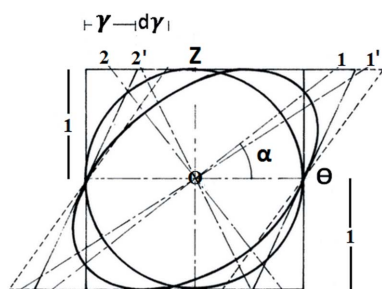

Figure 8
Experimental shear textures at equivalent strains of 5 for (*a*) grains No. 1 and No. 2, (*b*) grain No. 3, and (*c*) the rest of the space ($\varphi_2 = 45°$ sections of the ODF), obtained by 3D-EBSD scan.

Figure 9
Theoretical plane strain representation of a simple shear problem: an initial recrystallized grain is considered as a circle inscribed within a square. After employment of a shear strain of γ, the circle deforms to an ellipse where 1 and 2 represent its major and minor axes, respectively. An additional incremental shear strain of $d\gamma$ results in incremental rotation of the axes towards the shear direction.

parallelogram. The directionality of the ellipse towards the shear direction could be calculated using

$$\tan 2\alpha = 2/\gamma, \tag{2}$$

α being the angle between the major axis of the ellipse and the shear direction, and γ the shear strain. The relationship between the shear strain and the equivalent strain is determined by equation (1). Calculation of the strain along the principal axes allows estimation of the ratio between the major and the minor axes of the ellipsoid by equation (3):

$$\frac{a}{c} = \frac{1}{2}\left[\gamma^2 + 2 + \gamma(\gamma^2 + 4)^{1/2}\right]. \tag{3}$$

If we assume plane strain deformation this leads to the conclusion that the angle between the major axis of an ellipsoid and the shear direction completely lies in the Θ–Z plane, *i.e.* there is no inclination towards the r direction. The validity of this assumption has been examined at a strain level of 10.

Fig. 10(a) illustrates a schematic representation of an arbitrary grain, where a, b and c stand for the major, middle and minor lengths of the ellipsoid, respectively. At a strain of 10, the spatial distribution of the ellipsoids' axes with respect to cylindrical coordinates is represented in a pole-figure-like map (Fig. 10b). Inspection of this map confirms that the middle axis of an average ellipsoid is almost parallel to the radial direction
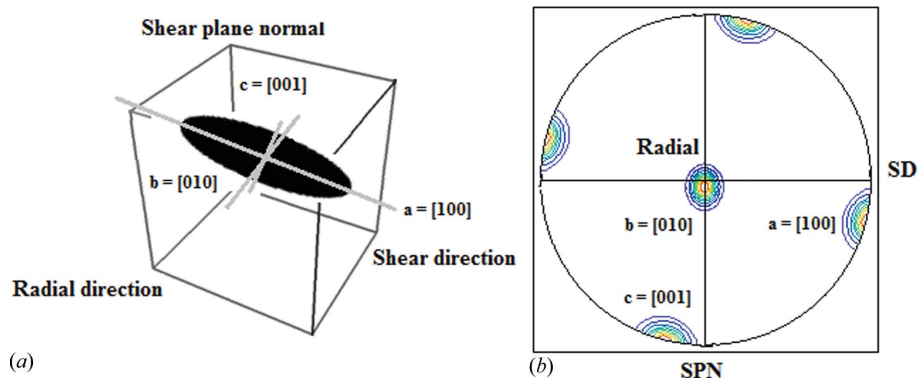
and the inclination between the major axis of an average fitted ellipsoid and the shear direction only lies in the Θ–Z plane.

Statistical analysis of the ellipsoid shapes (Table 2) suggests that the Θ–Z plane contains the highest morphological anisotropy, *i.e.* the a/c ratio is the largest number. On the other hand, the plane built by the radial direction and the major axis of the ellipsoid has the least morphological anisotropy, *i.e.* the a/b ratio is the smallest number. This explains why grains look more equi-axed from the top surface observations (Pippan *et al.*, 2010). It is concluded that grains display an oblate shape in space, with a specific inclination towards the shear direction. This inclination is smaller in the fragmentation stage, and gradually grows to a value of about 20° in the saturation regime, while equation (2) predicts a continuously decreasing value with strain (*cf.* Fig. 5). Indeed, the difference between experimental and theoretical a/c ratios at a strain of 5 is a direct consequence of grain fragmentation. While the theoretical a/c ratio grows considerably with straining, the experimental value saturates at a strain of 10. It is reported that in ECAP-processed copper this discrepancy can be explained by the CDRX process (Skrotzki Scheerbaum, Oertel, Arruffat-Massion *et al.*, 2007). The possibility of effective occurrence of DRX in low-purity aluminium is discussed here.

The GB migration rate is believed to control the type of DRX process, and its value is reported to be considerably smaller in CDRX than in DDRX. If the time needed for transformation of a subgrain boundary into a large-angle GB is significantly smaller than the time required for a mobile GB to sweep a distance equal to the microstructure size, DDRX is suppressed and CDRX becomes probable (Chovet *et al.*, 2000; Montheillet & Le Coze, 2002). This time difference is reflected in the recrystallized microstructure: the local density of dislocations tends to zero after DDRX, while the presence of dislocations is quite distinct after CDRX. Indeed, the presence of a very recognizable dislocation structure at different stages of deformation is confirmed in our investigation, *e.g.* the average kernel misorientation of about 1.1° at a strain of 5 is typical of a minimum density of geometrically necessary dislocations of about 4×10^{13} m^{-2}. In the fragmentation stage, the refinement of grains follows a pattern of gradual increase of misorientation by accumulation of dislocations, and formation of HAGBs as an extension of LAGBs (Naghdy, Kesten *et al.*, 2016). This arrangement might be explained by properties of the crystallographic rotation field for simple shear deformation which has the potential to transform LAGBs into HAGBs. This suggests that the CDRX process might be of relevance in the fragmentation stage, while DDRX is not the prevalent mechanism.

Vorhauer & Pippan (2008) reported, in a study on Armco iron processed by monotonic HPT, that the grain shape in the saturation regime is affected by the

(a)

(b)

Figure 10
(a) Schematic representation of a reconstructed shape of an individual grain with an ellipsoid; (b) distribution of the orientation of the ellipsoids' axes ($a > b > c$) at an equivalent strain of 10.

Soroosh Naghdy *et al.* · 3D-EBSD study of pure aluminium   **1519**

processing temperature: the higher the temperature, the more equi-axed the microstructure. The authors attribute this type of microstructure to isotropic movement of atoms at GBs, while a preferential movement of atoms is needed to explain the directionality of the microstructure at lower temperatures. It is suggested that, owing to the difficulty of medium-distance diffusion at the low-temperature regime, GB movement in the steady-state stage is governed by high stresses (Pippan *et al.*, 2010). *In situ* tensile TEM experiments on a nanocrystalline high-purity aluminium film at room temperature provide interesting information (Legros *et al.*, 2008). It is reported that grains close to a stress concentration, due to an unwanted crack, showed a considerable growth from 90 nm to about 700 nm. Loading led to migration of GBs and grains grew to a size of about 1.6 µm in this region. The authors distinguished two different types of GB migration: slow with an average growth speed of 0.2 nm s^{-1} and fast with an average speed of 50 nm s^{-1}. The former is associated with a diffusion-induced process, while the latter is linked with athermal shear.

Mobility of GBs in diffusion-controlled GB migration mechanisms is thermally activated and defined by an Arrhenius equation:

$$M = M_0 \exp\left(-\frac{Q}{RT}\right), \qquad (4)$$

where M_0 is a constant, R is the gas constant, T is the temperature and Q is the activation energy for diffusion. It is reported that Q is a function of the specific character of the GB. In the analysis of the GB migration rate during hot-deformation-regime DRX, the value of Q is assumed to be equal to the activation energy of bulk diffusion and diffusion along GBs for LAGBs and HAGBs, respectively (Gourdet & Montheillet, 2002; Montheillet & Le Coze, 2002). The activation energy for self-diffusion and GB diffusion in commercial purity aluminium is 155 and 80 kJ mol^{-1}, respectively (Gourdet & Montheillet, 2002). It is reported that an applied stress promotes this thermally activated process, and migration energies decrease but remain comparable to volume and GB diffusion energies for LAGBs and HAGBs, respectively (Winning *et al.*, 2001).

In the following, experimental data related to the motion of $\langle 100 \rangle$ symmetric tilt boundaries in high-purity aluminium bicrystals is used to approximate the deformation needed to account for the observed inclination of grains with respect to the shear direction in our investigation. To this purpose, generated heat of deformation is taken into account, and it is assumed that the orientation of the GB with respect to the applied stress is optimal, *i.e.* a maximum amount of stress is applied on the plane. Using the parameter list of Table 5, equation (4) leads to a predicted GB speed of 0.6 nm s^{-1}. It has to be noted that internal stresses as well as external stresses cause movement of the GBs. Capillary forces arising from the small curvature of GBs and accumulation of dislocations in pile-ups contribute to these internal stresses. The nature of GBs in our study is more complex than that of $\langle 100 \rangle$ symmetric tilt GBs, which belong to a more mobile planar family. The existence of a random orientation of GBs with

Table 5
List of parameters used to calculate the speed of $\langle 100 \rangle$ planar GBs (σ_y and Hv represent the yield strength and hardness of the material, respectively).

Q at room temperature (Winning & Rollett, 2005)	65 kJ mol^{-1}
M_0 (Winning & Rollett, 2005)	0.44 ± 0.04 m s^{-1} MPa^{-1}
ΔT rise of temperature (Edalati *et al.*, 2011)	10 K
Saturated microhardness (Ito *et al.*, 2017; Ito & Horita, 2009; Naghdy, Percq *et al.*, 2016)	50 ± 2 Hv
$\alpha = \sigma_y/Hv$ (Zhang *et al.*, 2011)	2.9 ± 0.05

respect to stress makes the predicted GB speed smaller in reality. Therefore, the obtained speed serves as an upper bound for a diffusional mechanism. In the saturation regime, at a radius of 3 mm and a rotational speed of 1 r min^{-1}, if the GB migration speed is 0.6 nm s^{-1} then a shear strain of 50 is required to account for translation of an average ellipsoid's major axis from the horizontal position to 20° inclination. The average speed of GBs in our investigation is not known, but the measurements at shear strain intervals of 1, between equivalent strains of 10 and 15, demonstrate the consistency of the inclination angle. In other words, the speed of GB migration is at least 50 times faster than what a diffusional mechanism might cause. The inability of a diffusion-induced GB migration mechanism to account for fast translation of atoms as demonstrated in our study may be explained by a shear-coupled grain-growth mechanism.

The calculated minimum densities of GNDs in our study are 4×10^{13} and 2.2×10^{13} m^{-2} in the fragmentation and saturation stages, respectively. The larger density of GNDs in the fragmentation stage could be correlated with the grain-refinement mechanism. Indeed, during high-pressure tube twisting of pure copper, a difference of five orders of magnitude was observed in the GND densities between the fragmentation and saturation stages (Pougis *et al.*, 2014). The authors argued that this deficit corresponds to a much lower CDRX rate in the saturation regime. Additionally, it is reported that in the steady-state stage some grain-boundary movement takes place, leading to DDRX. This process is believed to increase the size of a few grains above the limiting size needed for them to be subdivided by a further CDRX process (Pougis *et al.*, 2014; Toth & Gu, 2014).

In our study, however, the density of GNDs in the saturation regime does not decrease that drastically. This suggests that the CDRX mechanism might have been active in both deformation stages. Additionally, we assume a cycle which could account for the occurrence of a steady state in the saturation regime. It is suggested that a shear-coupled grain-growth mechanism may lead to an increase of the average grain size. Following the growth of grains, CDRX may take place to further refine the grain size. The combination of these two phenomena could account for a steady state and explain the near equality of GND densities in the fragmentation and saturation stages.

4.2. Texture evolution

Owing to the geometry of the specimen and the symmetry of the experiment, HPT-processed samples show a monoclinic

type symmetric texture with the radial direction, the r axis, as the monoclinic axis (Van Houtte & Aernoudt, 1976). The ideal monoclinic symmetry implies that the pairs of orientations $(A, \overline{A})$ and $(B, \overline{B})$ exhibit the same intensity, while (A_1^*, A_2^*) can grow independently, because of their asymmetrical nature. The initial recrystallized material shows a strong texture with a TI value of 4.91, and this has evolved to a considerably weaker texture with a TI value of 1.69 after a strain of 5. The sharp decline of TI might be explained by substantial grain fragmentation that has occurred at this level of deformation. The equivalent growth of symmetrically identical components of $(A, \overline{A})$ and $(B, \overline{B})$ is well displayed in the ODFs of Fig. 6. Further increase of deformation to a strain of 10 leads to development of an even weaker texture with a TI value of 1.38. The TI decrease between strain levels 5 and 10 is translated into a decrease of the intensity of the ideal components in the ODFs. This weaker texture might be attributed both to the role of grain fragmentation and to the nature of deformation, since simple shear does not produce any absolute stable ending point for orientations in Euler space. A similar texture is observed at a strain level of 50, with a somewhat weaker TI value of 1.30.

The evolution of texture in the saturation regime is affected by different potentially active deformation mechanisms in UFG materials, such as dislocation glide, twinning and GBS. Each of these deformation mechanisms has a specific effect on texture evolution. In the case of twinning, slip ocurs by involvement of partial dislocations and therefore a transition from the so-called copper-type to brass-type texture is observed (Gu *et al.*, 2014). It has been shown that GBS results in either a shift from the ideal positions of the deformation texture (Skrotzki *et al.*, 2013) or a massive randomization of the texture (Ivanisenko *et al.*, 2010). Examination of Fig. 6 confirms that no apparent shift takes place in the position of the ideal components. Moreover, the quantitatively similar ODFs at strains of 10 and 50 indicate that the weakening of the texture has already occurred before the saturation regime. This suggests that twinning and GBS are not the main deformation mechanisms in the saturation regime. The minor decrease of the TI between strain levels of 10 and 50 could be attributed to the rigid-body rotation which takes place in simple shear deformation.

3D-EBSD results at a strain level of 5 provide very interesting information about the interaction of grain fragmentation and texture evolution (*cf.* Fig. 8). It is observed that grains No. 1 and No. 2 are precisely located on the B fiber and fulfill the monoclinic symmetry condition, *i.e.* both components of B and $\overline{B}$ are present. The concurrent presence of symmetrically equivalent components of B and $\overline{B}$ prevents a local concentration of stress and secures a regional stability. The maxima of the ODFs show that grain No. 3 has the strongest orientation amongst the larger grains, and it appears in very close proximity to the ideal C position. The resistance of these three grains to fragmentation might be explained by their orientations. The amount of lattice rotation that a grain would experience is affected by its distance from the closest ideal position. It is expected that orientations which are initially

closer to ideal positions would rotate less, while orientations which are farther from the stable fibers experience larger lattice rotations. Therefore, a less severe fragmentation for the former seems more likely. The $\varphi_2 = 45°$ ODF section of heavily fragmented orientations is shown in Fig. 8(*c*). Comparison of Fig. 8(*c*) with Fig. 6(*a*) suggests that the local texture suffers from lack of symmetry, *i.e.* component $\overline{B}$ is absent. Inspection of Fig. 8(*c*) reveals that between the observed orientation and the ideal B position a misorientation exists of 10° around the radial axis. The observation of this misorientation in the more heavily fragmented zones and its absence in the larger grains suggest that the initial discrepancy from the ideal position was larger in the former.

The orientation-dependent subdivision pattern was studied by Quey *et al.* (2012) during plane strain compression tests on an aluminium polycrystal composed of 176 individual grains at 673 K. The properties of the reorientation velocity field were analyzed and the fragmentation pattern was correlated with the symmetry of orientations. In agreement with the results of the current study, crystal plasticity finite element simulations showed that the unstable orientations are more prone to fragmentation. These orientations are aligned with respect to the sample symmetry axes and therefore are positioned on the bifurcation lines of the velocity field. Subsequently, they rotate in two symmetrically opposite directions, resulting in grain subdivision.

The effect of the intragranular microstructure which develops during deformation is taken into account in a fragmentation crystal plasticity model proposed by Tóth *et al.* (2010). This model accounts for the role of lattice distortion and assumes that the concomitant rotation of the crystal-lographic planes of the crystallite is impeded near the grain boundaries. Consequently, the misorientation between neighboring subgrains may increase and a new grain boundary may appear. An additional feature of this model is the prediction of the grain-refinement intensity for different orientations. The model predicts a lower and higher fragmentation rate for orientations in the vicinity of and far away from ideal positions, respectively.

In the following, the fragmentation behavior of orientations close to and far from ideal positions is studied separately by calculating the grain size distribution for orientations within a 10° tolerance from ideal fibers and outside this zone (*cf.* Fig. 11). It was observed that orientations in the vicinity of ideal fibers have a larger average grain size in comparison to non-ideal orientations. This corroborates the results of 3D-EBSD measurement, *i.e.* the fragmentation is more effective for unstable orientations. This is in agreement with the prediction by Tóth *et al.* (2010). Moreover, a quantification of grain fragmentation in cold-rolled aluminium showed that the orientation gradient was much larger for three non-ideal orientations (Delannay *et al.*, 2001). The same behavior was observed during cold rolling of iron (Raabe, 1994). It was found that orientation gradients were absent in the stable $\{001\}\langle110\rangle$ component and prominent in the unstable $\{011\}\langle211\rangle$ component. This effect is attributed to the role of lattice rotation. The orientations which are in the immediate
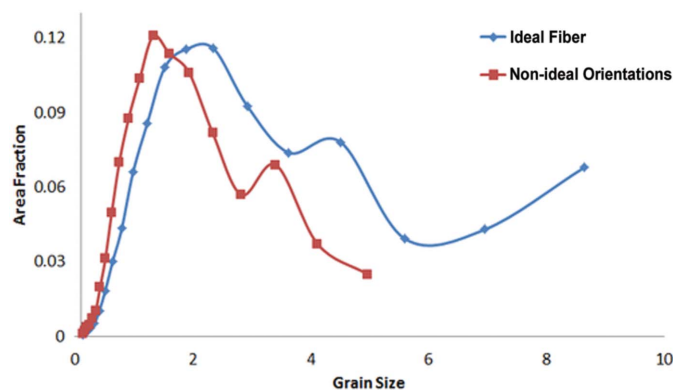
Figure 11
Grain size distribution at a strain of 5 using a large-area EBSD scan, showing that orientations in the vicinity of ideal fibers have a larger average grain size.

vicinity of ideal positions experience less lattice rotation. This explains the observation of a relatively larger average grain size for ideal orientations.

5. Conclusions

The morphological and crystallographic anisotropy of commercially pure aluminium during room temperature HPT was studied by conventional and three dimensional EBSD. The following conclusions can be drawn:

(1) The saturated microstructure does not appear equi-axed in all directions. The microstructure is morphologically anisotropic in the Θ–Z plane, as the grains show an elongated shape in this plane, while they appear more equi-axed in the r–Θ plane.

(2) Experimental results show that the grains' long axes are $\sim 20°$ inclined towards the shear direction. A directional migration of atoms is needed to explain this behavior.

(3) The process of refinement of grains during the grain fragmentation stage follows a pattern of gradual increase of misorientation and transformation of LAGBs to HAGBs. This phenomenon may be explained by the features of the CDRX mechanism.

(4) In the steady-state stage, a fast movement of atoms is needed to account for the translation of the grains' major axis. A purely diffusion-based GB migration mechanism could not produce the required velocity. A shear-coupled grain-growth mechanism is suggested as a possible mechanism to explain this phenomenon.

(5) A cyclic mechanism is proposed for the occurrence of a steady state in the saturation regime. It is suggested that a shear-coupled grain-growth mechanism may lead to an increase of the average grain size. Following the growth of grains, CDRX may take place to refine the grain size. The combination of the CDRX and the stress-induced grain-growth mechanisms could produce a steady state in the substructure.

(6) Since neither a shift in the position of ideal components nor a massive texture randomization have been observed, GBS does not play a significant role in the steady-state stage.

(7) A preferential fragmentation behavior was observed: fragmentation is more effective for orientations that are farther from ideal positions. Grains in the vicinity of ideal positions, however, are less fragmented. This difference was explained by lattice rotation experienced by each orientation during deformation.

References

Babcock, S. & Balluffi, R. (1989). *Acta Metall.* **37**, 2357–2365.
Bachmaier, A., Hafok, M. & Pippan, R. (2010). *Mater. Trans.* **51**, 8–13.
Barnett, M. R. & Montheillet, F. (2002). *Acta Mater.* **50**, 2285–2296.
Cahn, J. W., Mishin, Y. & Suzuki, A. (2006). *Acta Mater.* **54**, 4953–4975.
Cahn, J. W. & Taylor, J. E. (2004). *Acta Mater.* **52**, 4887–4898.
Caillard, D., Mompiou, F. & Legros, M. (2009). *Acta Mater.* **57**, 2390–2402.
Canova, G., Shrivastava, S., Jonas, J. & G'Sell, C. (1982). *Formability of Metallic Materials 2000 A.D.*, ASTM Special Technical Publication 753, edited by J. R. Newby & B. A. Niemeier, pp. 189–210. Philadelphia: American Society for Testing and Materials.
Chinh, N. Q., Szommer, P., Csanádi, T. & Langdon, T. G. (2006). *Mater. Sci. Eng. A*, **434**, 326–334.
Chovet, C., Gourdet, S. & Montheillet, F. (2000). *Mater. Trans. JIM*, **41**, 109–112.
Delannay, L., Mishin, O. V., Jensen, D. J. & Van Houtte, P. (2001). *Acta Mater.* **49**, 2441–2451.
Edalati, K., Miresmaeili, R., Horita, Z., Kanayama, H. & Pippan, R. (2011). *Mater. Sci. Eng. A*, **528**, 7301–7305.
Fukutomi, H., Iseki, T., Endo, T. & Kamijo, T. (1991). *Acta Metall. Mater.* **39**, 1445–1448.
Gianola, D. S., Van Petegem, S., Legros, M., Brandstetter, S., Van Swygenhoven, H. & Hemker, K. J. (2006). *Acta Mater.* **54**, 2253–2263.
Gourdet, S. & Montheillet, F. (2002). *Acta Mater.* **50**, 2801–2812.
Gourdet, S. & Montheillet, F. (2003). *Acta Mater.* **51**, 2685–2699.
Gu, C. F., Toth, L. S., Zhang, Y. D. & Hoffman, M. (2014). *Scr. Mater.* **92**, 51–54.
Haessner, F. & Schmidt, J. (1993). *Acta Metall. Mater.* **41**, 1739–1749.
Hallberg, H., Wallin, M. & Ristinmaa, M. (2010). *Mater. Sci. Eng. A*, **527**, 1126–1134.
Haslam, A. J., Moldovan, D., Yamakov, V., Wolf, D., Phillpot, S. R. & Gleiter, H. (2003). *Acta Mater.* **51**, 2097–2112.
Hohenwarter, A., Bachmaier, A., Gludovatz, B., Scheriau, S. & Pippan, R. (2009). *Int. J. Mater. Res.* **100**, 1653–1661.
Huang, Y. & Langdon, T. G. (2003). *Mater. Sci. Eng. A*, **358**, 114–121.
Ito, Y., Edalati, K. & Horita, Z. (2017). *Mater. Sci. Eng. A*, **679**, 428–434.
Ito, Y. & Horita, Z. (2009). *Mater. Sci. Eng. A*, **503**, 32–36.
Ivanisenko, Y., Skrotzki, W., Chulist, R., Lippmann, T., Yang, K., Kurmanaeva, L. & Fecht, H.-J. (2010). *J. Mater. Sci.* **45**, 4571–4577.
Jonas, J. J. & Aranas, C. Jr (2014). *IOP Conf. Ser. Mater. Sci. Eng.* **63**, 012048.
Kaibyshev, R. O., Mazurina, I. A. & Gromov, D. A. (2006). *Met. Sci. Heat Treat.* **48**, 57–62.

Kassner, M. & Evangelista, E. (1995). *Microstructural and Crystallographic Aspects of Recrystallization*, pp. 383–391. Risø National Laboratory.

Kawasaki, M. (2014). *J. Mater. Sci.* **49**, 18–34.

Kocks, U. F., Tomé, C. N. & Wenk, H.-R. (2000). Editors. *Texture and Anisotropy: Preferred Orientations in Polycrystals and Their Effect on Materials Properties*. Cambridge University Press.

Kozlov, E. V., Zhdanov, A. N., Popova, N. A., Pekarskaya, E. E. & Koneva, N. A. (2004). *Mater. Sci. Eng. A*, **387–389**, 789–794.

Langdon, T. G. (2013). *Acta Mater.* **61**, 7035–7059.

Legros, M., Gianola, D. S. & Hemker, K. J. (2008). *Acta Mater.* **56**, 3380–3393.

Li, L., Ungár, T., Toth, L. S., Skrotzki, W., Wang, Y. D., Ren, Y., Choo, H., Fogarassy, Z., Zhou, X. T. & Liaw, P. K. (2016). *Metall. Mater. Trans. A*, **47**, 6632–6644.

Molodov, D. A., Ivanov, V. A. & Gottstein, G. (2007). *Acta Mater.* **55**, 1843–1848.

Mompiou, F., Caillard, D. & Legros, M. (2009). *Acta Mater.* **57**, 2198–2209.

Montheillet, F. & Le Coze, J. (2002). *Phys. Status Solidi (A)*, **189**, 51–58.

Naghdy, S., Kestens, L., Hertelé, S. & Verleysen, P. (2016). *Mater. Charact.* **120**, 285–294.

Naghdy, S., Percq, L. L., Serret, R., Petrov, R., Hertelé, S., Kestens, L. & Verleysen, P. (2016). *Mater. Sci. Technol.* **33**, 678–687.

Orlov, D., Bhattacharjee, P. P., Todaka, Y., Umemoto, M. & Tsuji, N. (2009). *Scr. Mater.* **60**, 893–896.

Pippan, R., Scheriau, S., Taylor, A., Hafok, M., Hohenwarter, A. & Bachmaier, A. (2010). *Annu. Rev. Mater. Res.* **40**, 319–343.

Pougis, A., Toth, L. S., Fundenberger, J. J. & Borbely, A. (2014). *Scr. Mater.* **72–73**, 59–62.

Quey, R., Dawson, P. R. & Driver, J. H. (2012). *J. Mech. Phys. Solids*, **60**, 509–524.

Raabe, D. (1994). *Phys. Status Solidi (B)*, **181**, 291–299.

Sakai, T., Miura, H. & Yang, X. (2009). *Mater. Sci. Eng. A*, **499**, 2–6.

Samajdar, I., Verlinden, B., Rabet, L. & Van Houtte, P. (1999). *Mater. Sci. Eng. A*, **266**, 146–154.

Setman, D., Schafler, E., Korznikova, E. & Zehetbauer, M. J. (2008). *Mater. Sci. Eng. A*, **493**, 116–122.

Shan, Z. W., Stach, E. A., Wiezorek, J. M. K., Knapp, J. A., Follstaedt, D. M. & Mao, S. X. (2004). *Science*, **305**, 654–657.

Sheikh-Ali, A. D. & Szpunar, J. A. (1998). *Mater. Sci. Eng. A*, **245**, 49–54.

Skrotzki, W., Eschke, A., Jóni, B., Ungár, T., Tóth, L. S., Ivanisenko, Y. & Kurmanaeva, L. (2013). *Acta Mater.* **61**, 7271–7284.

Skrotzki, W., Scheerbaum, N., Oertel, C.-G., Arruffat-Massion, R., Suwas, S. & Tóth, L. S. (2007). *Acta Mater.* **55**, 2013–2024.

Skrotzki, W., Scheerbaum, N., Oertel, C.-G., Brokmeier, H.-G., Suwas, S. & Tóth, L. S. (2007). *Acta Mater.* **55**, 2211–2218.

Tóth, L. S., Estrin, Y., Lapovok, R. & Gu, C. (2010). *Acta Mater.* **58**, 1782–1794.

Toth, L. S. & Gu, C. (2014). *Mater. Charact.* **92**, 1–14.

Tóth, L. S., Jonas, J. J., Daniel, D. & Bailey, J. A. (1992). *Textures Microstruct.* **19**, 245–262.

Tóth, L. S., Neale, K. W. & Jonas, J. J. (1989). *Acta Metall.* **37**, 2197–2210.

Valiev, R. Z., Islamgaliev, R. K. & Alexandrov, I. V. (2000). *Prog. Mater. Sci.* **45**, 103–189.

Valiev, R. Z., Ivanisenko, Y. V., Rauch, E. F. & Baudelet, B. (1996). *Acta Mater.* **44**, 4705–4712.

Van Houtte, P. (2004). *The MTM-FHM Software System*, Katholieke Universiteit Leuven, Belgium.

Van Houtte, P. & Aernoudt, E. (1976). *Mater. Sci. Eng.* **23**, 11–22.

Van Swygenhoven, H., Derlet, P. M. & Hasnaoui, A. (2002). *Phys. Rev. B*, **66**, 024101.

Van Swygenhoven, H., Spaczer, M. & Caro, A. (1999). *Acta Mater.* **47**, 3117–3126.

Vorhauer, A. & Pippan, R. (2008). *Metall. Mater. Trans. A*, **39**, 417–429.

Winning, M. (2007). *Philos. Mag.* **87**, 5017–5031.

Winning, M., Gottstein, G. & Shvindlerman, L. S. (2001). *Mater. Sci. Eng. A*, **317**, 17–20.

Winning, M. & Rollett, A. D. (2005). *Acta Mater.* **53**, 2901–2907.

Xu, C., Furukawa, M., Horita, Z. & Langdon, T. G. (2003). *Acta Mater.* **51**, 6139–6149.

Zhang, J., Gao, N. & Starink, M. J. (2011). *Mater. Sci. Eng. A*, **528**, 2581–2591.

Zhilyaev, A. P. & Langdon, T. G. (2008). *Prog. Mater. Sci.* **53**, 893–979.

Zhilyaev, A. P., Lee, S., Nurislamova, G. V., Valiev, R. Z. & Langdon, T. G. (2001). *Scr. Mater.* **44**, 2753–2758.

Zhu, Y. T., Liao, X. Z. & Wu, X. L. (2012). *Prog. Mater. Sci.* **57**, 1–62.